

PHYSICAL REVIEW A

GENERAL PHYSICS

THIRD SERIES, VOL. 6, No. 2

AUGUST 1972

Cascade-Decoupling Measurements of Excited S -State Hyperfine Structures of Potassium, Rubidium, and Cesium†

R. Gupta, S. Chang, and W. Happer
Columbia Radiation Laboratory, Department of Physics,
Columbia University, New York, New York 10027
(Received 17 March 1972)

A new cascade-decoupling technique has been used to measure hyperfine intervals (in MHz) of the following excited S states of alkali-metal atoms: $K^{39}(6^2S_{1/2}) 46 \pm 2$; $K^{41}(6^2S_{1/2}) 26 \pm 2$; $Rb^{85}(7^2S_{1/2}) 270 \pm 10$; $Rb^{85}(8^2S_{1/2}) 135 \pm 15$; $Rb^{87}(7^2S_{1/2}) 565 \pm 60$; $Rb^{87}(8^2S_{1/2}) 290 \pm 20$; $Cs^{133}(8^2S_{1/2}) 680 \pm 120$; and $Cs^{133}(9^2S_{1/2}) 405 \pm 30$.

I. INTRODUCTION

Recently¹ we reported preliminary measurements of excited S -state hyperfine-structure (hfs) intervals in potassium, rubidium, and cesium. The alkali-metal atoms are, perhaps, the most simple many-electron atoms in the periodic system, since their low-lying spectra are due principally to the motion of a single valence electron around the nucleus and closed shells of core electrons. However, excitations of the core do have a significant influence on many atomic parameters, such as hfs coupling constants, fine structure, and oscillator strengths. Thus, the properties of alkali-metal atoms form natural test cases for modern many-body computational techniques. In this paper, we present extensive new measurements of excited S -state hyperfine structures in the alkali-metal atoms, and we hope these data will stimulate a more careful theoretical analysis of hyperfine structure in the alkali atoms.

Until recently, precision measurements of hyperfine structure in the alkali-metal atoms have been limited almost exclusively to the ground state and to the excited P states. The ground-state hfs intervals have been measured with very high precision by atomic-beam techniques, and in fact, the present time standard is defined in terms of the ground-state hyperfine interval of Cs^{133} . With few exceptions, the excited-state hfs intervals are smaller than the Doppler widths of optical lines, and conventional optical spectroscopy cannot be used for precision measurements. However, the excited-state hfs intervals of alkali-metal atoms are often

considerably larger than the natural widths of the states. Consequently, optical-double-resonance² and level-crossing spectroscopy,³ which have a resolution limited mainly by the natural width of the state, have been extensively used to measure the properties of the excited P states of alkali atoms. Unfortunately, conventional optical-double-resonance or level-crossing techniques cannot be used to investigate the properties of excited S states, D states, and F states, since these states cannot be produced by direct optical excitation of ground-state alkali atoms.

The optically inaccessible S , D , and F states can be produced by electron excitation, and Archambault *et al.*⁴ have investigated some of the D states in sodium and cesium with electron excitation. However, they were only able to set rather rough limits on the hyperfine structures of these states. Electron excitation cannot produce a polarized S state unless polarized electrons or polarized target atoms are used. In some of our early work⁵ we produced polarized excited S -state atoms by electron excitation of optically pumped alkali-metal vapors in a weak electrical discharge. We did not pursue these experiments because of the difficulty of applying large radio-frequency fields to a weakly ionized plasma. We should mention that Pavlovic and Laloë⁶ have successfully used electron excitation of polarized He^3 atoms to investigate the hyperfine structure of a number of excited states of He^3 . Kibble and Pancharatnam⁷ and Smith and Eck⁸ have used stepwise optical excitation to reach inaccessible states in mercury and lithium. Stepwise exci-

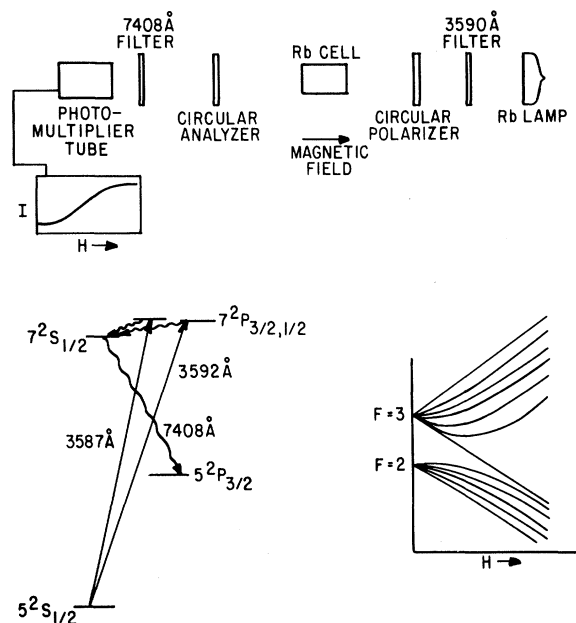


FIG. 1. A typical cascade-decoupling experiment to measure the hyperfine interval of the optically inaccessible $7^2S_{1/2}$ state of Rb^{85} . Circularly polarized 3587- and 3592-Å resonance lines from a Rb-vapor lamp are used to populate the $7P$ levels of Rb vapor. Electronic polarization of the $7^2S_{1/2}$ state, produced by cascade transitions from the $7P$ levels, is detected by monitoring the circular polarization of the 7408-Å fluorescent radiation (lower left-hand side). The increase in the intensity I of circularly polarized light is related to the Breit-Rabi diagram (lower right-hand side) for the $7^2S_{1/2}$ state. A more detailed sketch of the apparatus is shown in Fig. 8.

tation seems very promising, although it requires intense and carefully designed lamps to produce an adequate number of atoms in the intermediate state.

In this paper we present the results of hyperfine-structure measurements in eight excited S states of potassium, rubidium, and cesium. We have found that the inaccessible S and D states can be conveniently populated by cascade transitions from higher-lying P states, which are excited by polarized resonance radiation. For example, the experimental arrangement for investigating the $7^2S_{1/2}$ state of rubidium is shown in Fig. 1. The third resonance line of rubidium (3587 and 3592 Å) is used to excite the $7P$ state of rubidium vapor. Some of the $7P$ atoms decay to the $7S$ state. If the ultraviolet exciting light is circularly polarized, part of the photon's angular momentum is passed on to the $7S$ state when the $7P$ state decays. After a mean lifetime of about 100 nsec, the $7S$ state decays and some of the atoms fall into the $5^2P_{3/2}$ state and emit 7408-Å fluorescent light. The circular polarization of this 7408-Å light is measured as a function of the

strength of a longitudinal external magnetic field H . As Fig. 1 indicates, the circular polarization increases with H . The field dependence is reminiscent of the Hanle effect, but the physical origin is somewhat different. The field dependence of the circular polarization is mainly due to the decoupling of the nuclear spin I from the electronic spin J of the $7S$ state, and the width, ΔH (in G), of the curve is approximately

$$\Delta H \approx h\Delta\nu/g_J\mu_B.$$

In contrast to the Hanle effect,⁹ the excited-state lifetime has little influence on the shape of the curve, provided that the hyperfine period is much less than the natural lifetime of the state.

The mechanism of the decoupling is illustrated in Fig. 2. Suppose that an excited atom is created with its electronic angular momentum J directed along the magnetic field H , and suppose that the nuclear spin I is pointing in some random direction at the instant of creation. Then the subsequent behavior of the atom depends on the strength of the magnetic field. At low magnetic fields ($g_J\mu_B H \ll h\Delta\nu$), I and J precess around each other at the hyperfine frequency $\Delta\nu$ to form a resultant angular momentum F . The total angular momentum F slowly precesses around the small magnetic field. The mean z component of electronic angular momentum $\langle J_z \rangle$ is therefore smaller than the initial value J . At high magnetic fields ($g_J\mu_B H \gg h\Delta\nu$), I and J are decoupled and J remains locked to the large magnetic field while I precesses independently. Thus, at high fields the mean z component of electronic angular momentum remains equal to its initial value. Since the circular polarization of the fluorescent light is proportional to $\langle J_z \rangle$ for the emitting atom, we expect the circular polarization to increase as the magnetic field increases.

The first decoupling experiments seem to have been performed by Ellet and Heydenburg¹⁰ in studies of the hyperfine structure of excited states of sodium and cesium. Similar techniques have been used to measure the hyperfine structure of muonium,¹¹ and recently Pavlovic and Laloë⁶ have used electron excitation of polarized He^3 atoms, in conjunction with decoupling techniques, to measure the hyperfine structure of many excited states of He^3 . Although the accuracy of the decoupling method probably does not exceed a few percent, the method has a number of important advantages with respect to radio-frequency spectroscopy. First, the decoupling method is very simple; no high-power radio-frequency generators are required, and large sample cells can be used. Second, the signal-to-noise ratios of decoupling experiments are typically 5 to 10 times larger than the signal-to-noise ratios of radio-frequency spectroscopy. Consequently, one must integrate 25 to 100 times longer in an rf ex-

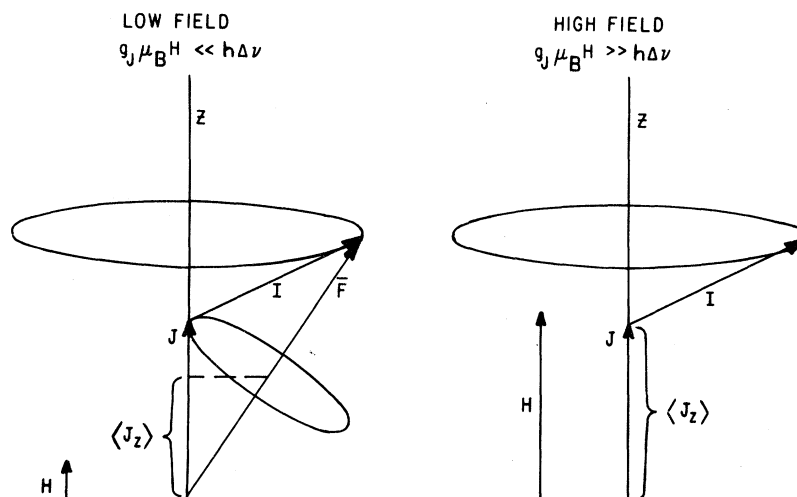


FIG. 2. The decoupling mechanism. Suppose that excited atoms are created with a longitudinal electronic spin J and a nuclear spin I which can point in any random direction. At low fields (left-hand side), I and J couple to each other and some of the longitudinal electronic angular momentum is transformed into longitudinal nuclear angular momentum. At high fields (right-hand side) J remains locked to H , and I precesses independently. No longitudinal electronic angular momentum is transferred to I . The circular polarization of light emitted by the atoms is proportional to the longitudinal *electronic* angular momentum, and the circular polarization is therefore larger at high fields than at low fields.

periment to obtain a signal-to-noise ratio equal to that of a decoupling experiment. Finally, the decoupling signal is actually better in an atom with a large nuclear spin than in an atom with a small nuclear spin, since a large nuclear spin can absorb more electronic angular momentum at low fields. This is in sharp contrast to rf spectroscopy, where a large nuclear spin is usually detrimental to the signal-to-noise ratio, since it increases the number of sublevels in which the atom may be found. Decoupling spectroscopy yields information on atomic states with no high-field level crossings,¹² such as the $^2S_{1/2}$ states which are discussed in this paper. Eck¹³ has pointed out that the decoupling signal can be regarded as a superposition of many zero-field anticrossing signals. The decoupling measurements greatly simplify subsequent high-precision radio-frequency spectroscopy, since they provide good initial estimates of the transition frequencies and signal strengths. One can therefore search for the rf resonances in a very narrow frequency interval. We have completed radio-frequency measurements¹⁴ of some of the S-state intervals reported in this paper, and we find excellent agreement with the decoupling results.

A precise theoretical analysis of cascade-fluorescence experiments is presented in Sec. II. The details of our experimental apparatus are presented in Sec. III, and our results and conclusions are discussed in Sec. IV.

II. THEORY OF CASCADE-FLUORESCENCE EXPERIMENTS

The theory of cascade-fluorescence experiments is similar to the theory of level-crossing spectro-

scopy.¹² However, the cascading step adds some complications which do not seem to have been adequately discussed in the literature, and we will therefore give a brief but complete derivation of the theory of cascade-fluorescence experiments here.

Four atomic states are involved in the experiment (see Fig. 3), and we shall call these states g (ground), e (excited), b (branch), and f (final). We assume that the atom has a nuclear spin I . Because

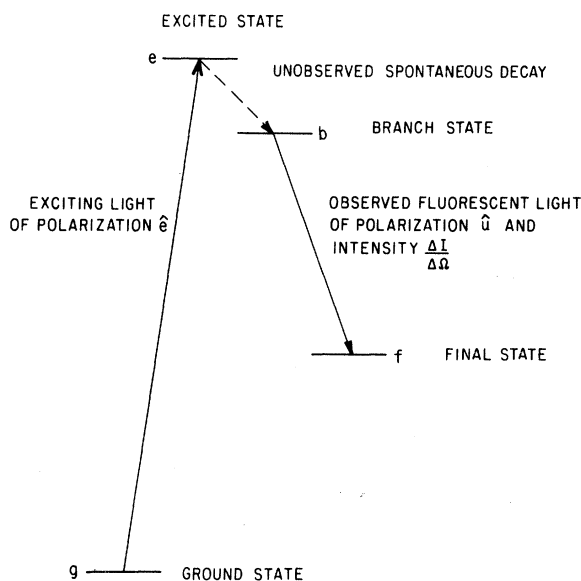


FIG. 3. The atomic states involved in a cascade-fluorescence experiment.

of the coupling of I to the electronic spin J , hyperfine structure will exist in each of the atomic states. We shall designate the electronic angular momenta in the ground, excited, branch, and final states by J_g , J_e , J_b , and J_f , respectively. Ground-state atoms are transferred into the excited state by a beam of polarized resonance radiation. Excited-state atoms decay spontaneously into the branch state, but we do not observe the infrared fluorescent radiation which is produced by the decay $e \rightarrow b$. Branch-state atoms decay spontaneously to the final state, and we do observe the polarized fluorescent light which is produced by the decay $b \rightarrow f$. The goal of the theory is to calculate the dependence of the fluorescent light intensity on the properties of the four atomic states of Fig. 3.

A. Evolution of Atomic States

It is convenient to describe the distribution of atoms among the sublevels of an atomic state of angular momentum J with a density matrix ρ . The evolution of the density matrix is described by

$$\frac{d}{dt} \rho = \frac{1}{i\hbar} [\mathcal{H}, \rho] - \Gamma \rho + S. \quad (1)$$

The evolution due to hyperfine interactions and external fields is governed by the Hamiltonian

$$\mathcal{H} = hA \vec{I} \cdot \vec{J} + hB \left(\frac{3(\vec{I} \cdot \vec{J})^2 + \frac{3}{2} \vec{I} \cdot \vec{J} - I(I+1)J(J+1)}{2I(2I-1)J(2J-1)} \right) + g_J \mu_B H J_z + g_I \mu_B H I_z. \quad (2)$$

Here A and B are, respectively, the magnetic dipole and electric quadrupole hfs coupling constants of the state. The gyromagnetic ratios of the electronic and nuclear angular momenta are g_J and g_I , respectively, H is the magnitude of an external magnetic field, directed along the z axis, and μ_B is the Bohr magneton. The atom decays spontaneously at a rate Γ , where $\tau = \Gamma^{-1}$ is the total radiative lifetime of the state. The atoms are produced at a rate S , where S might represent optical excitation from a lower state or cascade excitation from an upper state. In general, S will be a matrix with the same dimensions as ρ . Let us discuss optical excitation and cascade excitation in more detail.

B. Optical Excitation

If we assume that the frequency profile of the exciting light is flat in the neighborhood of the hyperfine components of the absorption line $g \rightarrow e$ (see Fig. 3), we can use Fermi's "Golden rule" to write the source term for the excited state as

$$S(e) = 2\pi \left(\frac{e}{m\omega_{eg}\hbar} \right)^2 u \hat{e} \cdot \vec{p} \rho_g \hat{e}^* \cdot \vec{p}. \quad (3)$$

Here ρ_g is the ground-state density matrix, \hat{e} is the polarization vector of the exciting light, \vec{p} is the

momentum operator of the atom, and u is the energy density of the light ($\text{erg cm}^{-3} \text{Hz}^{-1}$) in the neighborhood of the resonance frequency ω_{eg} .

In all of the experiments reported in this paper, the ground-state atoms were completely unpolarized. We shall therefore limit our attention to unpolarized ground-state density matrices of the form

$$\rho_g = (2I+1)^{-1} (2J_g+1)^{-1} \sum_{\mu} |g\mu\rangle \langle g\mu|, \quad (4)$$

where the sum extends over all ground-state sublevels $|g\mu\rangle$. If we substitute (4) into (3), we can use angular momentum recoupling rules (see, for instance, the Appendix of Ref. 15) to write

$$S(e) = 3R(2I+1)^{-1} \sum_L (-1)^L W(J_g J_e 1 L; 1 J_e) \times E_L \cdot T_L(J_e J_e), \quad (5)$$

where the mean excitation rate R is

$$R = \pi e^2 f u / m \omega_{eg} \hbar, \quad (6)$$

and f is the absorption oscillator strength of the transition $g \rightarrow e$. The irreducible tensors E_{LM} and T_{LM} are discussed in detail in the Appendix of Ref. 15. The basis operators are

$$T_{LM}(JJ) = \sum_m |Jm\rangle \langle Jm-M| (-1)^{m-M-J} \times C(JJL; m, M-m), \quad (7)$$

and the polarization tensors E_{LM} are defined in terms of the components of the polarization vector \hat{e} as

$$E_{LM} = \sum_m e_m (e_{m-M})^* (-1)^{m-M-1} C(11L; m, M-m). \quad (8)$$

Equation (5) indicates that only electronic polarization is generated by broad-line excitation from an unpolarized ground state. No nuclear polarization is initially present in the excited atom, but some of the electronic polarization can be transformed into nuclear polarization if the atom lives long enough, and if the coupling between I and J is stronger than the coupling of J to the external magnetic field.

C. Cascade Excitation

The source term for the population of the branch state b by spontaneous decay of the excited state e can be obtained with Fermi's Golden rule. We find

$$S(b) = \frac{4e^2 \omega_{eb}}{3m^2 c^3 \hbar} \vec{p} \cdot \rho_e \vec{p}, \quad (9)$$

where ρ_e is the density matrix of the excited state and ω_{eb} is the frequency of the transition $e \rightarrow b$. Equation (9) is analogous to (3), and it differs only because we have replaced the real energy density u by the "energy density" $2\hbar \omega_{eb}^3 / \pi c^3$ of the vacuum fluctuations and we have averaged over all possible polarizations of the emitted photons, which introduces a factor of $\frac{1}{3}$.

For future reference, we note that an important special case of (9) is

$$\frac{4e^2\omega_{eb}}{3m^2c^3\hbar}\vec{p}\cdot T_{LM}(J_eJ_e)\vec{p} \\ = T_{LM}(J_bJ_b)\Gamma_{eb}(2J_e+1)W(1J_eJ_bL; J_bJ_e). \quad (10)$$

Here Γ_{eb} is the partial decay rate from e to b . Equation (10) signifies that the rate of generation of the electronic multipole moment $T_{LM}(J_bJ_b)$ of the branch state is proportional to the corresponding electronic multipole moment $T_{LM}(J_eJ_e)$ of the excited state. Hence, electronic polarization can be partially transferred from state to state by cascading. The nuclear polarization is not changed at all by spontaneous decay.

D. Fluorescence

All of the experimental data in this paper were obtained by observing the intensity and polarization of the fluorescent light which is emitted during the decay of the branch state to the final state. One can use Fermi's Golden rule to show that the intensity ΔI of fluorescent light emitted into the small solid angle $\Delta\Omega$ is

$$\Delta I = \text{Tr}[\rho_b\mathcal{L}]\Delta\Omega, \quad (11)$$

where the fluorescent-light operator \mathcal{L} is

$$\mathcal{L} = \frac{e^2\omega_{bf}}{2\pi m^2c^3\hbar} \sum_{\nu} \hat{u}\cdot\vec{p}|f\nu\rangle\langle f\nu|\vec{p}\cdot\hat{u}^*. \quad (12)$$

Here \hat{u} is the polarization vector of the fluorescent light, ρ_b is the density matrix of the branch state, and the units of (11) are photons per second. Since the sum in (12) extends over all sublevels $|f\nu\rangle$ of the final state, any complete set of sublevels can be used, and it is not necessary that the $|f\nu\rangle$ be eigenstates of the atom. Consequently, the fluorescent light intensity is independent of the hyperfine structure of the final state. This comes about because, in deriving (11) and (12), we have assumed that the photodetector is equally sensitive to all frequency components of the fluorescent light.

For future reference, we note that (12) can be written in spherical tensor form as

$$\mathcal{L} = \frac{3\Gamma_{bf}}{8\pi} (2J_b+1) \sum_L (-1)^L W(1LJ_fJ_b; 1J_b) \\ \times U_L T_L(J_bJ_b). \quad (13)$$

Here Γ_{bf} is the partial decay rate from b to f and the tensors U_{LM} are constructed from the polarization vector \hat{u} of the fluorescent light in analogy to (8). Physically, Eq. (13) indicates that only the *electronic* polarization of the branch state has any influence on the fluorescent light. The nuclear polarization of the branch state has no effect on the intensity and polarization of the fluorescent light.

Of course, this follows from our assumption that the photodetector for the fluorescent light is equally sensitive to all hyperfine frequency components of the light.

In the experiments reported in this paper, we are interested in ${}^2S_{1/2}$ branch states and ${}^2P_{1/2}$ or ${}^2P_{3/2}$ final states. In a branch state with $J_b = \frac{1}{2}$, the maximum multipolarity of the electronic polarization is $L = 1$, and (13) reduces to

$$\mathcal{L} = \mathcal{L}_0 + \mathcal{L}_1 \vec{t} \cdot \vec{J}. \quad (14)$$

Here \vec{J} is the electronic angular momentum operator in the branch state and \vec{t} is the mean spin of the detected photons ($t_x = -\sqrt{2}U_{10}$, etc.). The constants \mathcal{L}_0 and \mathcal{L}_1 can be obtained from (13), and they are listed in Table I for the two possible values of the final-state electronic angular momenta in our experiments.

At this point we would like to emphasize an important limitation of fluorescence monitoring of ${}^2S_{1/2}$ states. In the lighter alkali atoms, the ${}^2P_{1/2}$ and ${}^2P_{3/2}$ final states differ very little in energy, and the wavelengths of the two decay modes to these states are nearly the same. For instance, in sodium the wavelength of the $5{}^2S_{1/2} - 3{}^2P_{3/2}$ transition is 6161 Å, while the wavelength of the $5{}^2S_{1/2} - 3{}^2P_{1/2}$ transition is 6154 Å. It is impossible to separate these closely spaced lines with conventional interference filters, which have bandwidths on the order of 50 Å. Suppose that an imperfect filter has been used to isolate the fluorescent light, so that some photons corresponding to decays to both the ${}^2P_{1/2}$ and ${}^2P_{3/2}$ final states are detected. Denote the over-all quantum efficiencies for the two decay modes by η_1 and η_2 , respectively, and assume that the mean photon spin \vec{t} is the same for both modes. Then, using (11), (14), and Table I, we find that the net photon counting rate is

$$\eta_1\Delta I_1 + \eta_2\Delta I_2 = [(\eta_1\Gamma_1 + \eta_2\Gamma_2) \\ + (2\eta_1\Gamma_1 - \eta_2\Gamma_2)\langle\vec{J}\rangle\cdot\vec{t}](\Delta\Omega/8\pi). \quad (15)$$

The polarization-dependent part of (15) (the term proportional to $\langle\vec{J}\rangle\cdot\vec{t}$) is multiplied by a factor approximately equal to $\Gamma_2(\eta_1 - \eta_2)$, since, at least for light alkali atoms, we expect to find $\Gamma_2 \approx 2\Gamma_1$ (the statistical weight of the ${}^2P_{3/2}$ state is twice that of the ${}^2P_{1/2}$ state). Thus, the signal will be independent of the branch-state polarization if $\eta_1 = \eta_2$, that

TABLE I. Fluorescent light operator, $\mathcal{L} = \mathcal{L}_0 + \mathcal{L}_1 \vec{t} \cdot \vec{J}$, for a spin- $\frac{1}{2}$ state. The decay rate to the final state is Γ .

Final-state angular momentum	$\frac{8\pi}{\Gamma}\mathcal{L}_0$	$\frac{8\pi}{\Gamma}\mathcal{L}_1$
$\frac{1}{2}$	1	2
$\frac{3}{2}$	1	-1

is, if the quantum efficiencies of the two decay modes are equal. Since all of the interesting information about hyperfine structure is contained in the polarization-dependent term, we see that the hyperfine structure of a $^2S_{1/2}$ state can be measured only if one of the two decay modes can be detected with greater quantum efficiency (or with a different mean spin) than the other.

It is usually preferable to detect the decay mode to the $^2P_{1/2}$ state, since the polarization-dependent parts of the $^2P_{1/2}$ and $^2P_{3/2}$ signals are equal in magnitude (assuming $\Gamma_2 = 2\Gamma_1$), but the polarization-independent part of the $^2P_{3/2}$ mode is twice as large as the polarization-independent part of the $^2P_{1/2}$ mode. Thus, the shot noise will be about 40% greater for the $^2P_{3/2}$ mode than for the $^2P_{1/2}$ mode. Also, in the heavier alkali atoms the wavelength of the $^2P_{1/2}$ mode is substantially shorter than that of the $^2P_{3/2}$ mode, and one can obtain a worthwhile gain in quantum efficiency by observing the $^2P_{1/2}$ mode.

E. Steady-State Solutions

We can now derive expressions for the steady-state intensity of fluorescent light in a cascade-decoupling experiment. In this section we derive an exact, but cumbersome expression for the fluorescent intensity, and we discuss some of the peculiarities of the cascade-decoupling method for hyperfine-structure measurements in the excited $^2S_{1/2}$ states of alkali atoms. In Sec. II F, we derive a greatly simplified analytic expression for the fluorescent intensity.

Denote the energy difference between a pair of excited-state sublevels m and n by $\hbar\omega_{mn}$ and denote the energy difference between a pair of branch-state sublevels j and k by $\hbar\omega_{jk}$. Then, setting the left-hand side of (1) equal to zero, and taking matrix elements of both sides of the equation, we obtain the steady-state density matrix for the excited state,

$$\rho_{mn} = \frac{S_{mn}(e)}{\Gamma_e + i\omega_{mn}}. \quad (16)$$

A similar equation holds for the branch state

$$\rho_{jk} = \frac{S_{jk}(b)}{\Gamma_b + i\omega_{jk}}. \quad (17)$$

Combining Eqs. (12), (11), (17), (9), (16), (3), and (4), we find that the intensity of fluorescent light is

$$\begin{aligned} \frac{\Delta I}{\Delta\Omega} = & \frac{4}{3} \left(\frac{e}{mc} \right)^6 \frac{u}{\hbar^4} \frac{\omega_{eb}\omega_{bf}}{(\omega_{ge})^2} \frac{1}{(2J_g+1)(2I+1)} \\ & \times \sum_{\substack{m \\ n \\ jk \\ \mu\nu}} \langle j | \vec{p} | m \rangle \cdot \langle n | \vec{p} | k \rangle \langle k | \hat{u} \cdot \vec{p} | f\nu \rangle \langle f\nu | \hat{u}^* \cdot \vec{p} | j \rangle \\ & \times \langle m | \hat{e} \cdot \vec{p} | g\mu \rangle \langle g\mu | \hat{e}^* \cdot \vec{p} | n \rangle \end{aligned}$$

$$\times (\Gamma_e + i\omega_{mn})^{-1} (\Gamma_b + i\omega_{jk})^{-1}. \quad (18)$$

Equation (18) is quite similar to the Breit-Frank formula¹² for conventional level-crossing experiments. The fluorescent light intensity is independent of the hyperfine structure in the ground state and in the final state, but it does depend on the hyperfine structures of both the excited state and the branch state. Equation (18) contains the product of two resonance denominators, one for level crossings in the excited state and one for level crossings in the branch state, while the Breit-Frank formula contains only one resonance denominator (for the excited state). Also (18) contains the product of six dipole matrix elements, while the Breit-Frank formula contains the product of only four dipole matrix elements. Physically, the presence of two resonance denominators in (18) means that high-field level crossings will be difficult to observe in cascading experiments unless level crossings occur at the same field, within their natural width, in both the excited state and in the branch state. Furthermore, the azimuthal quantum numbers of the crossing excited-state levels must differ by exactly the same amount Δm , as the azimuthal quantum numbers of the crossing branch-state levels. Thus, pronounced high-field level-crossing signals should be a much rarer phenomenon in cascading experiments than in conventional level-crossing experiments without cascading. Zero-field level crossings (the Hanle effect) and anticrossings, however, should be easily observable in cascading experiments.

The numerical evaluation of (18) is quite tedious, and we have written a computer program which automatically evaluates the right-hand side of (18) as a function of the external magnetic field, the nuclear spin, the electronic angular momenta of the ground, excited, branch, and final states, and the hyperfine coupling constants and lifetimes of the excited and branch states. A complete description of this program is presented elsewhere.¹⁶ Some typical computer calculations for Rb⁸⁷ are illustrated in Figs. 4 and 5. These curves correspond to the experimental situation sketched in Fig. 1, and the values of the atomic parameters used in the calculations are indicated on the figures. In Fig. 4, a decoupling curve for cascading through the $7^2P_{3/2}$ state is shown. The structure between 0 and 30 G is due to decoupling of I and J in the $7^2P_{3/2}$ state. Very little decoupling of the $7^2S_{1/2}$ state occurs at fields below 30 G. The slow increase in intensity between 30 and 200 G is due to decoupling of I and J in the $7^2S_{1/2}$ state. This type of behavior is actually observed, as the experimental data of Fig. 6 indicate. We should mention that our experimental curves were obtained with a rotating analyzer and phase-sensitive detection. The experimental

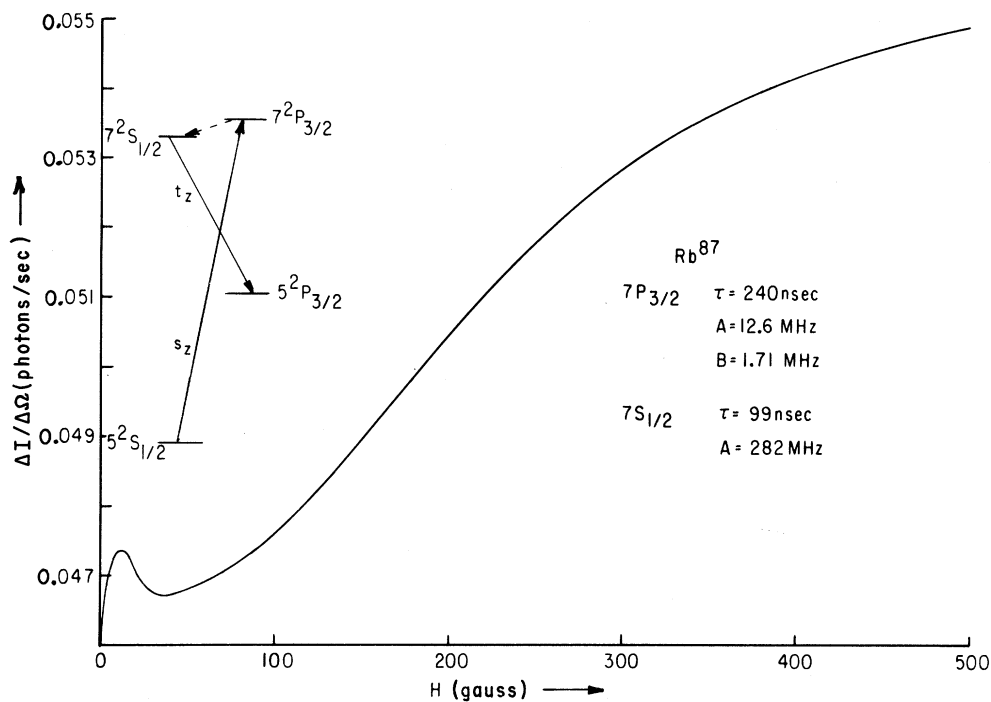


FIG. 4. Decoupling curve, calculated with Eq. (18) for cascading through the $7^2P_{3/2}$ state to the $7^2S_{1/2}$ state of Rb^{87} . The structure below 30 G is due to decoupling in the $7^2P_{3/2}$ state, and the structure above 30 G is due to decoupling in the $7^2S_{1/2}$ state.

signal of Fig. 6 is therefore proportional to $\langle J_z \rangle$. An additional polarization-independent field-independent signal is included in the theoretical curves

of Figs. 4 and 5. Only the field-dependent parts of the experimental and theoretical curves should be compared.

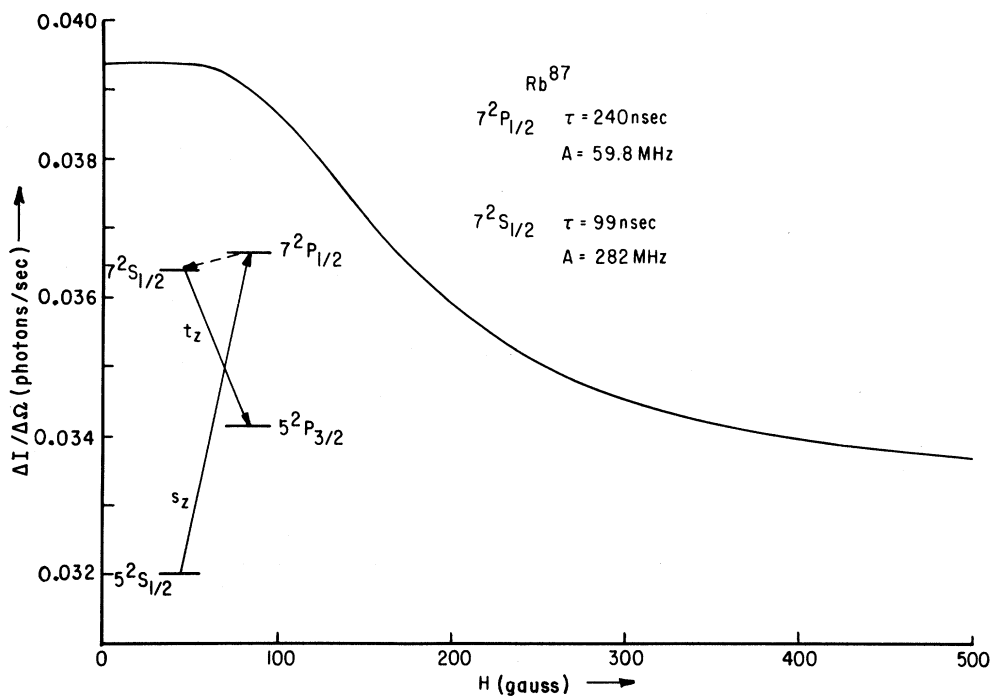


FIG. 5. Decoupling curve, calculated with Eq. (18) for cascading through the $7^2P_{1/2}$ state to the $7^2S_{1/2}$ state of Rb^{87} . The effects of P -state decoupling are not as striking as they are in Fig. 4.

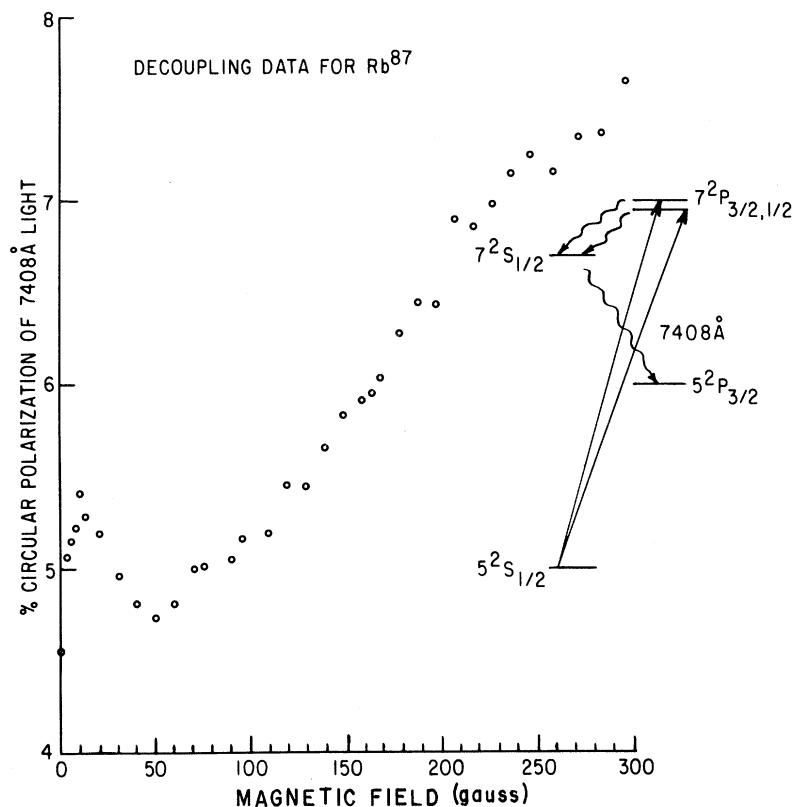


FIG. 6. Experimental decoupling data for the $7^2S_{1/2}$ state of Rb⁸⁷. The strong resemblance of this curve to the calculated curve of Fig. 4 indicates that the $7^2S_{1/2}$ state is mainly populated through the $7^2P_{3/2}$ state.

The calculated decoupling curve for cascading through the $7^2P_{1/2}$ state, Fig. 5, does not have the same shape as the experimental curve of Fig. 6. Although low-field structure due to decoupling in the $7^2P_{1/2}$ curve is present in Fig. 5, it is much less noticeable than the low-field structure in Fig. 4. Also, while the curve in Fig. 4 increases at high magnetic fields, the curve in Fig. 5 decreases at high magnetic fields. The signals due to cascading through the $2^2P_{1/2}$ and $2^2P_{3/2}$ states will therefore tend to cancel. Our experimental data (e.g., Fig. 6) indicate that the $2^2P_{3/2}$ route always dominates. Although we are usually not able to filter the closely spaced $2^2P_{1/2}$ and $2^2P_{3/2}$ components of the exciting light, there are at least three reasons that the $2^2P_{3/2}$ route may dominate. First, for equal pumping rates through the $2^2P_{1/2}$ and $2^2P_{3/2}$ states, the magnitude of the decoupling signal is bigger for the $2^2P_{3/2}$ route. This is evident from Figs. 4 and 5 and is discussed in more detail in Sec. II F in connection with Table II. Second, for equal intensities of pumping light at the excitation frequencies for the $2^2P_{1/2}$ and $2^2P_{3/2}$ excited states, the pumping rate into the $2^2P_{3/2}$ state is at least twice as large as the pumping rate into the $2^2P_{1/2}$ state, and for the heavier alkali atoms, the anomalous oscillator-strength ratio¹⁷ for the resonance line doublets enhances the $2^2P_{3/2}$ pumping rate even more. Finally, it would

not be surprising if the $2^2P_{3/2}$ component of the exciting light were more intense than the $2^2P_{1/2}$ component.

F. Approximate Analytic Solution

The computer-generated curves of Figs. 4 and 5 reproduce the observed results in all details, but they are inconvenient to work with, and rather costly in computer time. However, as Figs. 4 and 5 demonstrate, the high-field portions of the decoupling curves have a simple appearance. It is possible to obtain a fairly simple analytic expression which gives an excellent approximation to the exact high-field solutions.

Suppose that the magnetic field is large enough that m_I and m_J are approximately good quantum numbers in the 2^2P_J excited state. Furthermore, assume that pure circularly polarized light, propagating along the z direction, is used to excite the

TABLE II. Source matrix, $S=S_0+S_1s_zJ_z$, for excitation of $2^2S_{1/2}$ state by cascading through a 2^2P_J excited state.

Excited state	$\frac{2(2I+1)\Gamma_e S_0}{R\Gamma_{eb}}$	$\frac{6(2I+1)\Gamma_e S_1}{R\Gamma_{eb}}$
$2^2P_{1/2}$	1	-2
$2^2P_{3/2}$	1	+5

atom. Then the source matrix S of Eq. (3) will be diagonal in the energy representation of the excited state, and (16) becomes

$$\rho(e) = S(e)/\Gamma_e. \quad (19)$$

We may use the multipole expansion (5) for $S(e)$ to write (19) as

$$\rho(e) = 3R \Gamma_e^{-1} (2I+1)^{-1} \sum_L (-1)^L \times W(J_e J_e 1 L; 1 J_e) E_{L0} T_{L0}(J_e J_e). \quad (20)$$

Equation (20) implies that the excited P state has purely electronic polarization and an unpolarized nucleus. This follows from our assumption that the excited state was completely decoupled by the magnetic field and that the ground state was unpolarized. We should mention that (20) is actually valid for any polarization and propagation direction of the exciting light, provided that the electronic Larmor precession frequency ω of the excited atom greatly exceeds the natural decay rate. Under these conditions, one can retain only the longitudinal components of the source matrix, since the transverse components rotate many times during the excited-state lifetime and average to zero [i.e., the transverse components are smaller than the longitudinal components by a factor on the order of $\Gamma_e/(\Gamma_e + iM\omega)$, where M is the azimuthal angular momentum of the transverse component].

The source matrix for the branch state can be obtained from (20) by using (9) and (10), and we find

$$S(b) = 3R \Gamma_{e_b} \Gamma_e^{-1} (2I+1)^{-1} (2J_e+1) \sum_L (-1)^L \times W(J_e J_e 1 L; 1 J_e) W(1 J_e J_b L; J_e J_e) \times E_{L0} T_{L0}(J_b J_b). \quad (21)$$

Equation (21) implies that the branch-state atoms are also produced with longitudinal purely electronic polarization.

Since we are interested in $^2S_{1/2}$ branch states ($J_b = \frac{1}{2}$), the maximum multipolarity of the state is $L = 1$ and (21) can be written as

$$S(b) = S_0 + S_1 s_\pi J_\pi, \quad (22)$$

where the constants S_0 and S_1 , which can be obtained from (21), are listed in Table II; $s_\pi = -\sqrt{2}E_{10}$ is the mean longitudinal spin of the exciting photons, and $J_\pi = (1/\sqrt{2})T_{10}(J_b J_b)$ is the z component of the electronic angular momentum operator of the branch state. By substituting (22) into (17), we find that the steady-state density matrix for the branch state is

$$\rho_{jk} = \frac{S_0}{\Gamma_b} \delta_{jk} + S_1 s_\pi \frac{\langle j | J_\pi | k \rangle}{\Gamma_b + i\omega_{jk}}. \quad (23)$$

Combining (23) with (11) and (14), we find that the intensity of fluorescent light is

$$\frac{\Delta I}{\Delta \Omega} = 2(2I+1) \frac{S_0 \mathcal{L}_0}{\Gamma_b} + S_1 \mathcal{L}_1 s_\pi t_\pi \sum_{jk} \frac{|\langle j | J_\pi | k \rangle|^2}{\Gamma_b + i\omega_{jk}}. \quad (24)$$

In deriving (24) we have made use of the fact that

$$\sum_i \langle i | J_\pi | i \rangle = 0 \quad (25)$$

for any complete set of states $|i\rangle$. Since the steady-state density matrix (23) is longitudinal, only the longitudinal spin t_π of the detected photons influences the fluorescent intensity.

The magnetic field dependence of the fluorescent intensity (24) is proportional to the quantity

$$y = \frac{1}{2I+1} \sum_{jk} \frac{|\langle j | J_\pi | k \rangle|^2}{1 + i\tau_b \omega_{jk}}, \quad (26)$$

which occurs in the right-hand side of (24) and which may be thought of as the mean longitudinal electronic spin $\langle J_\pi \rangle$ which would be produced if the branch-state atoms were created with their electron spins 100% polarized along the positive z axis but with completely random nuclear spins. Subsequent coupling of I and J during the branch-state lifetime τ_b will tend to diminish the electronic polarization from its initial value of $\frac{1}{2}$ toward its mean value y .

Equation (26) can be evaluated with the Breit-Rabi formulas¹⁸ for the energies and eigenvectors of a spin- $\frac{1}{2}$ atom in an external magnetic field. The energy of the upper (+) and lower (-) states of total azimuthal quantum number m are

$$E(m \pm 1) = -\frac{1}{4}Ah + g_I \mu_B H m \pm \frac{1}{2}Ah(v^2 + z^2)^{1/2}, \quad (27)$$

where $(I + \frac{1}{2})A = \Delta\nu$ is the zero-field hyperfine interval, and the parameters v and z depend on m and are, respectively,

$$v^2 = (I + \frac{1}{2})^2 - m^2, \quad (28)$$

$$z = m + x(I + \frac{1}{2}). \quad (29)$$

The field parameter x is

$$x = \frac{\mu_B H(g_J - g_I)}{h\Delta\nu}. \quad (30)$$

The corresponding basis states are

$$|m+\rangle = Nv |m_J = \frac{1}{2}, m_I = m - \frac{1}{2}\rangle + N[(v^2 + z^2)^{1/2} - z] |m_J = -\frac{1}{2}, m_I = m + \frac{1}{2}\rangle \quad (31)$$

and

$$|m-\rangle = N[z - (z^2 + v^2)^{1/2}] |m_J = \frac{1}{2}, m_I = m - \frac{1}{2}\rangle + Nv |m_J = -\frac{1}{2}, m_I = m + \frac{1}{2}\rangle. \quad (32)$$

The normalizing constant is

$$N^2 = \frac{1}{2[v^2 + z^2 - z(v^2 + z^2)^{1/2}]}. \quad (33)$$

Using Eqs. (26)–(33), we find that the field dependence of the decoupling signals is

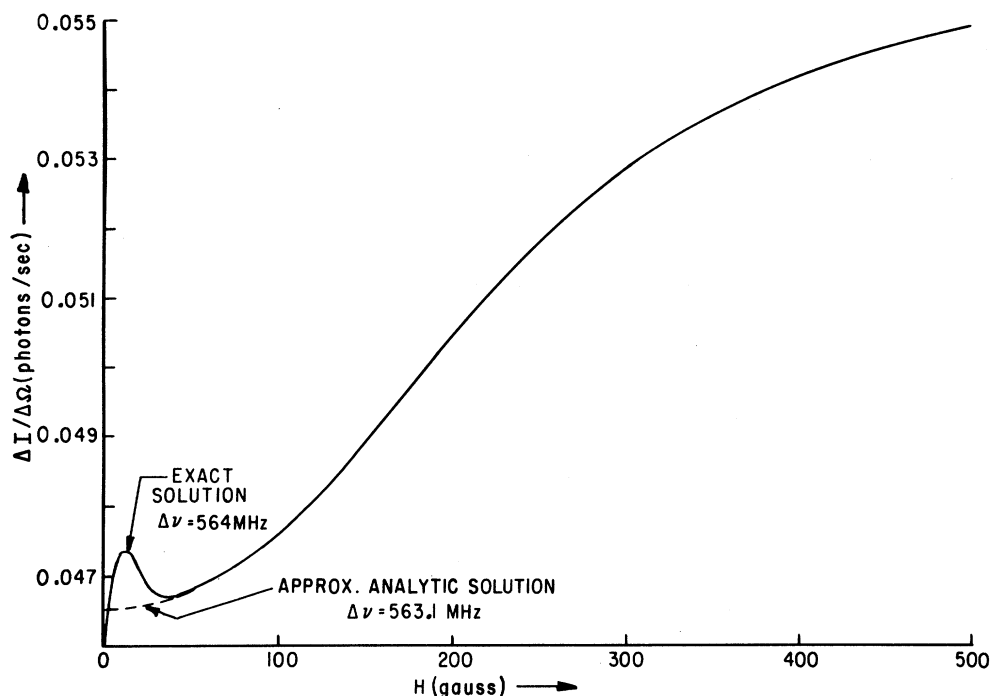


FIG. 7. A comparison of the exact decoupling curve for cascading through the ${}^2P_{3/2}$ state, calculated from Eq. (18), to the analytic decoupling curve, calculated from Eq. (34). The exact and analytic curves are almost identical outside of the region of P -state decoupling. The analytic curve was fitted by the method of least squares to the exact curve. The hyperfine interval was used as an adjustable parameter in the fit. These curves indicate that it is legitimate to use the much simpler analytic formula (34) instead of the exact formula (18) in fitting the experimental data.

$$y = \frac{1}{2(2I+1)} \left[1 + \sum_m \frac{1}{v^2 + z^2} \times \left(z^2 + \frac{v^2}{1 + [4\pi\Delta\nu\tau_b / (2I+1)]^2 (z^2 + v^2)} \right) \right]. \quad (34)$$

Equation (34) can be evaluated much more easily than the cumbersome Eq. (18), which gives the exact field dependence of the fluorescent light. A comparison of the analytic expression (34) to the exact expression (18) for cascading through in the ${}^2P_{3/2}$ state is shown in Fig. 7. The curves are hardly distinguishable except at very low magnetic fields, where the decoupling of the excited P state modifies the intensity of the fluorescent light. The agreement between the analytic and exact curves is less satisfactory for cascading through the ${}^2P_{1/2}$ state, but all experimental evidence indicates that the ${}^2P_{1/2}$ route is of negligible importance.¹⁶

III. APPARATUS

The apparatus we used to measure the polarization of the fluorescent radiation as a function of the magnetic field is shown schematically in Fig. 8. To investigate the $7{}^2S_{1/2}$ state of rubidium, a Pyrex cell containing rubidium vapor is illuminated with

circularly polarized third resonance lines (3587 and 3592 Å) from a rubidium lamp. The $7{}^2S_{1/2} \rightarrow 5{}^2P_{3/2}$ (7408 Å) fluorescent radiation from the cell passes through a circular polarization analyzer and is detected by a photomultiplier tube. A static magnetic field is maintained along the direction of the incident light by a pair of Helmholtz coils.

The rubidium lamp consists of a Pyrex bulb 2 in. in diameter and about 1 in. thick placed inside a microwave cavity. The bulb has a small amount of rubidium along with krypton gas at about 0.1-torr pressure. The cavity is externally heated to obtain sufficient rubidium-vapor pressure. The microwave power (from a commercial diathermy unit operating at 2450 MHz) is fed in toward the front end of the bulb. The most intense discharge is concentrated near the front end of the bulb, and the problem of the self-reversal of the emission lines is minimized. Owing to very small oscillator strengths for the third (and fourth) resonance lines, the self-reversal of the lines is not a serious problem. We empirically adjust the microwave power and the temperature of the bulb to obtain maximum 7408-Å fluorescence. The intensity of the third resonance lines (3587 and 3592 Å) from the lamp was measured to be about 5×10^{11} photons per second into a solid angle of 0.06 sr (roughly the solid angle subtended

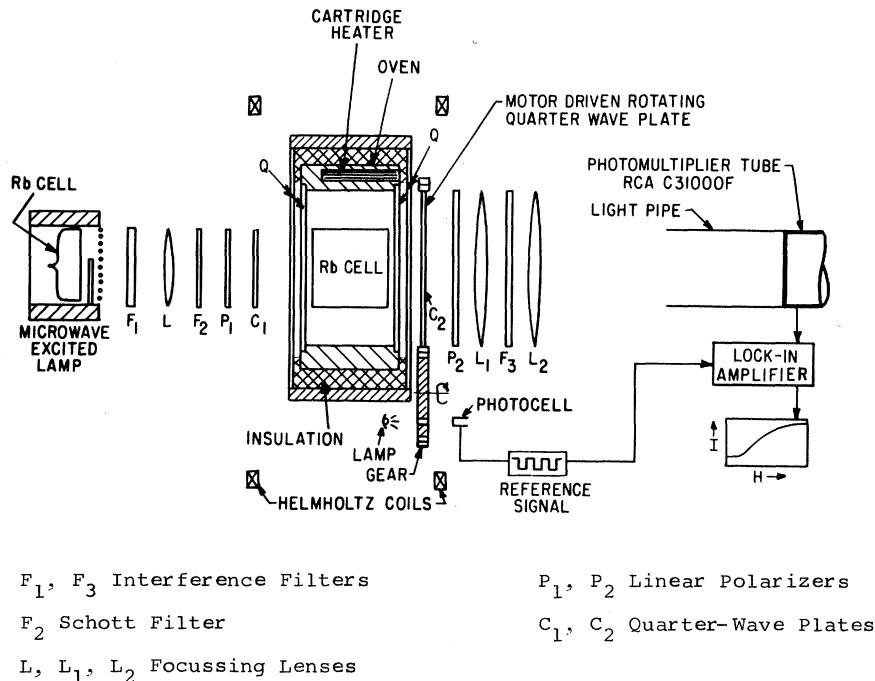


FIG. 8. A detailed diagram of our experimental arrangement. The reference signal for the phase-sensitive detector is obtained as shown. A Schott BG18 (1-mm-thick) colored-glass filter (which has a transmission of 50% at 3590 Å but transmits less than 0.001% in the near-infrared region) is used directly in front of the uv interference filter to minimize the leakage of much stronger near-infrared lines from the lamp into the PM tube. Two fresnel lenses in conjunction with a large (4×4 in.) interference filter are used to increase the solid angle subtended by the detector. Both lenses have equal focal lengths, and the distance between the center of the rubidium cell and L_1 is equal to their focal length. In this way, the light incident on the interference filter is made approximately parallel and high transmission at the peak wavelength is obtained. The photomultiplier tube is placed 75 cm from the center of the Helmholtz coils to avoid magnetic scanning of the gain. A light pipe is used to transmit the fluorescent light from the focal point of L_2 to the PM tube. F_1, F_3 are interference filters; F_2 is the Schott filter; L, L_1, L_2 are the focusing lenses; P_1, P_2 are the linear polarizers; and C_1, C_2 are the quarter-wave plates.

by the cell). We have tried several different types of lamps and this lamp seems to give maximum intensity of these lines.

The third resonance lines are selected with an interference filter. We do not filter the components of the fine-structure doublet, i. e., we use both $7^2P_{1/2} \rightarrow 5^2S_{1/2}$ and $7^2P_{3/2} \rightarrow 5^2S_{1/2}$ lines to excite the rubidium vapor. A Schott BG18 (1-mm-thick) colored-glass filter is used directly in front of the interference filter to minimize the leakage of the 7408-Å line from the lamp into the photomultiplier tube. The 7408-Å fluorescent radiation from the rubidium-vapor cell is selected by an interference filter. A large filter (4×4 in.) in conjunction with two focusing lenses is used (Fig. 8) to maximize the solid angle subtended by the detector. This solid angle is about 0.45 sr. The fluorescent light passes through a quarter-wave plate, a linear polarizer, and is detected by a dry-ice-cooled photomultiplier tube. The quarter-wave plate is mounted on a gear and is rotated by a synchronous motor. The circular polarization of the detected fluorescent

light is thus modulated at twice the frequency of revolution of the gear. The modulated signal is then detected with a phase-sensitive detector.

The rubidium-vapor cell is 2 in. in diameter and 2 in. thick. The temperature of the cell is empirically adjusted to give the optimum signal-to-noise ratio. This is accomplished in the following way: The total fluorescence and its degree of polarization are measured as a function of the cell temperature. While the total fluorescence continues to rise with rising temperature, its degree of polarization starts to decrease beyond a certain temperature. Figure 9 shows typical results for the $7^2S_{1/2}$ state of rubidium. The depolarization of the fluorescent radiation starts at about 125 °C for the $7^2S_{1/2}$ state of rubidium. We also find that the temperature at which the depolarization starts is independent of the thickness of the rubidium-vapor cell. Therefore, we believe, this effect is due to collisional depolarization in the excited states and not due to the trapping of the exciting light by the atoms. A systematic investigation of the collisional depolarization

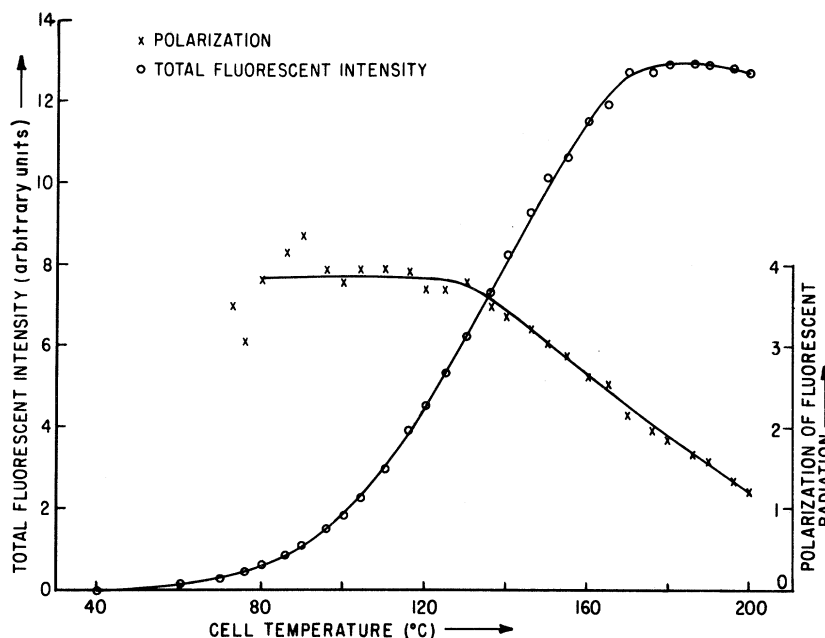


FIG. 9. Total fluorescent intensity and its degree of polarization as a function of the cell temperature for the case of Rb^{85} . Smooth lines have been drawn through the data points as a guide to the eye. Rubidium vapor was excited with circularly polarized $3590\text{-}\text{\AA}$ ($7^2P_{3/2,1/2} \rightarrow 5^2S_{1/2}$) radiation and the circularly polarized $7408\text{-}\text{\AA}$ ($7^2S_{1/2} \rightarrow 5^2P_{3/2}$) fluorescent radiation was observed. A weak magnetic field (2.5 G) was maintained along the direction of the incident light. At about 185°C the total fluorescent intensity starts to decrease, perhaps due to trapping of radiation by the atoms, quenching, or Lorentz broadening of the absorption profile. The depolarization of the fluorescent radiation at temperatures above 125°C is believed to be due to the collisional depolarization effects in the excited states, since the cell dimensions have little effect on the measured polarization-vs-temperature curves.

effects in the excited states is being carried out. For the $7^2S_{1/2}$ state, whose depolarization curve is illustrated in Fig. 9, we always operated with the cell at about 120°C (about 3×10^{13} atom/cm³). At this temperature, about 5×10^5 fluorescent photons per second were detected.

To investigate the $8^2S_{1/2}$ state in rubidium, the rubidium-vapor cell was illuminated with the fourth resonance lines (3349 and 3351 \AA) of rubidium and the polarization of the $8^2S_{1/2} \rightarrow 5^2P_{1/2}$ (6071 \AA) fluorescent radiation was measured as a function of the static magnetic field. Unfortunately, it was not possible to compensate for the low values of the oscillator strengths in these higher excited states by operating at higher vapor densities of rubidium. Instead, it was found that the depolarization of the 6071- \AA radiation started at considerably lower temperatures, presumably because the collisional depolarization cross sections are higher in the higher excited states. We operated the cell at about 100°C (approximately 7×10^{12} atom/cm³) and detected about 6×10^5 fluorescent photons per second.

For all of the other states that we have investigated, the basic apparatus is similar to that described above. The only changes are in the filters

used and the temperature of the cell. Table III gives a listing of the relevant parameters for all the states that we have investigated. The number of the fluorescent photons detected per second varied from those listed in Table III within approximately a factor of 2 from day to day, presumably because of changes in the lamp intensity. The Schott colored-glass filters proved to be very effective in minimizing the problem of the direct leakage of light from the lamp to the photomultiplier (PM) tube. This point is discussed further in Sec. IV. Column 5 of Table III lists the Schott filters that we have used.

IV. RESULTS AND CONCLUSIONS

Figure 10 shows the results of our measurements on the second excited S states of K^{39} , K^{41} , Rb^{85} , Rb^{87} , and Cs^{133} . Figure 11 shows similar data for the third excited S states of Rb^{85} , Rb^{87} , and Cs^{133} . The open circles are the experimental data points and the solid lines are the theoretical fits to these data based on (34). As pointed out in Sec. II, (34) correctly describes the shape of the decoupling signal at sufficiently high values of the magnetic field H such that I and J can be regarded as decoupled in the P states. In the least-squares analysis of the

TABLE III. A list of relevant parameters for various atomic states that were investigated in this work.

Element	State	Exciting light	Fluorescent light	Schott filter (s) used	Temperature of the cell °C	Vapor density in the cell (atoms/cm ³)	Typical number of fluorescent photons detected per second	Approximate observed magnitude of polarization of the fluorescent radiation	
								Low field (%)	High field (%)
K	$6^3S_{1/2}$	$6^2P_{1/2,3/2} \rightarrow 4^2S_{1/2}$ 3447 Å	$6^2S_{1/2} \rightarrow 4^2P_{1/2}$ 6911 Å	UG1 (2 mm)	150	2×10^{13}	7×10^5	1.5	3.5
		3448 Å							
Rb	$7^2S_{1/2}$	$7^2P_{1/2,3/2} \rightarrow 5^2S_{1/2}$ 3587 Å	$7^2S_{1/2} \rightarrow 5^2P_{3/2}$ 7408 Å	BG18 (1 mm)	120	3×10^{13}	6×10^5	7	18
		3592 Å							
Rb	$8^2S_{1/2}$	$8^2P_{1/2,3/2} \rightarrow 5^2S_{1/2}$ 3349 Å	$8^2S_{1/2} \rightarrow 5^2P_{1/2}$ 6071 Å	UG11 (1 mm) and BG38 (1 mm)	100	7×10^{12}	6×10^3	5.5	12.5
		3351 Å							
Cs	$8^2S_{1/2}$	$8^2P_{1/2,3/2} \rightarrow 6^2S_{1/2}$ 3876 Å	$8^2S_{1/2} \rightarrow 6^2P_{1/2}$ 7609 Å	BG18 (1 mm)	120	5×10^{13}	2×10^6	12.5	25
		3888 Å							
Cs	$9^2S_{1/2}$	$9^2P_{1/2,3/2} \rightarrow 6^2S_{1/2}$ 3611 Å	$9^2S_{1/2} \rightarrow 6^2P_{1/2}$ 6355 Å	UG1 (1 mm) and BG38 (2 mm)	85	7×10^{12}	7×10^3	5.5	12.5
		3617 Å							

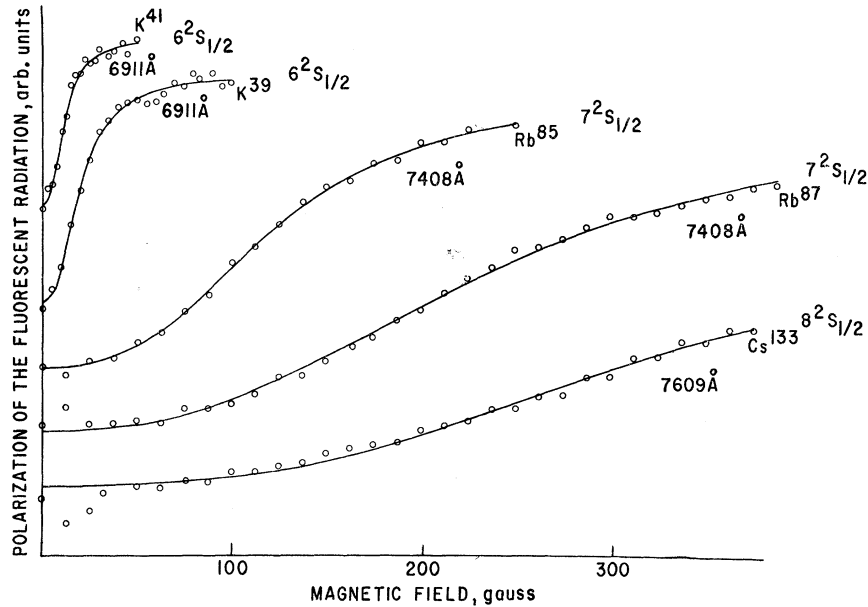


FIG. 10. Polarization of the fluorescent radiation from the second excited S states of various alkali-metal atoms as a function of the magnetic field. The circles are experimental points, and the solid lines are the theoretical fits to these data. The zero has been shifted by differing amounts for different curves, and each curve has a somewhat different vertical scale. Wavelengths of the observed fluorescent radiation are indicated on the figure. The large deviations of the experimental points from the theoretical curves at low fields are believed to be caused by decoupling of the P states.

data, we have ignored the data points at very low magnetic fields. Deviations of the data from the theoretical curves at low fields can readily be seen in Fig. 10. In our analysis, the quantity

$$\sum_i [y(H_i, \Delta\nu) - AP_{\text{expt}}(H_i) - B]^2$$

is minimized. Here y is calculated from (34) and P_{expt} is the experimental value of the polarization of the fluorescent light at a value of the magnetic field equal to H_i ; $\Delta\nu$ is the hyperfine frequency interval. The sum is taken over all the data points except the very low-field points. The three parameters A , B , and $\Delta\nu$ are varied to obtain the best fit. The multiplicative scaling factor A is required because we do not know the absolute values of the polarization. An additive factor B is required because a small but unknown amount of light leaks from the lamp into the photomultiplier tube.

The approximate observed magnitudes of the polarization of the 7408-Å radiation ($7^2S_{1/2} \rightarrow 5^2P_{3/2}$ for rubidium) range from about 7% at low magnetic fields to about 18% at high fields. The corresponding values of the polarization of the fluorescent radiation from the second excited S states of cesium and potassium are listed in Table III. We believe that the smaller polarization in the case of potassium is due, at least in part, to the poor filtering of the fine-structure components of the fluorescent radiation. As pointed out in Sec. II, the two fine-structure components have opposite polarization

and their intensity ratio is such that no net polarization would be observed if one component were not filtered out. Filtering of one fine-structure component in the case of potassium is difficult if a large solid angle of detection is required, since the two components are separated by only 28 Å. This is not a problem in the case of cesium and rubidium, as the fine-structure separation is much larger there. The considerable difference in the value of the polarization for rubidium and cesium is perhaps due to the fact that we have observed the $7^2S_{1/2} \rightarrow 5^2P_{3/2}$ fine-structure component of the fluorescence in the case of rubidium while the $8^2S_{1/2} \rightarrow 6^2P_{1/2}$ component has been observed for cesium. It will be recalled [Eq. (14)] that the polarizations for the two fine-structure components differ by a factor of 2. Another factor which may contribute to the differences in the observed values of the polarizations in potassium, rubidium, and cesium is the anomalous oscillator-strength ratio for the resonance line doublets of heavy alkali metals.¹⁷ Also, the efficiency of our polarizers varied with wavelength. The infrared quarter-wave plate used for the curves shown in Fig. 10 had a retardation value of (2000 ± 200) Å.

As pointed out earlier, we had to operate the cell at lower vapor densities for the investigation of the third excited states. This, combined with lower oscillator strengths for these states, decreased the signal-to-noise ratio considerably.

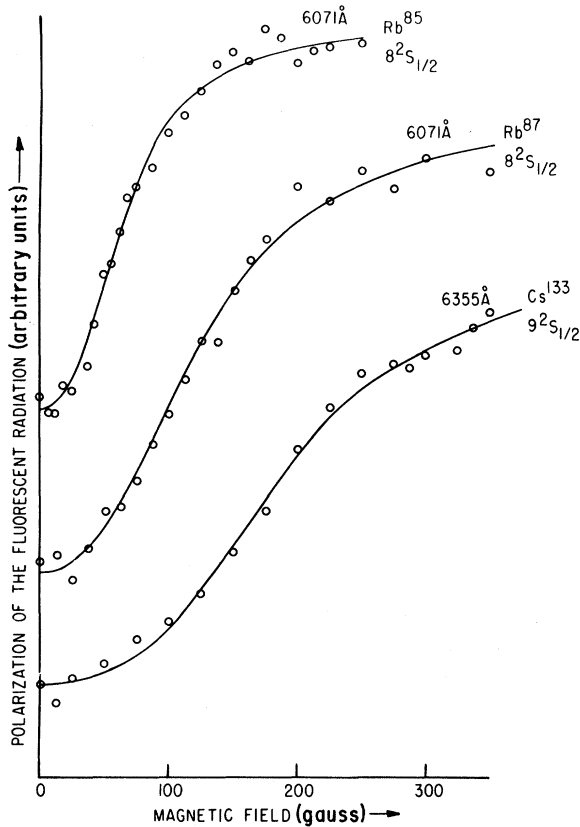


FIG. 11. Data similar to those of Fig. 10 for the third excited S states of rubidium and cesium. Solid lines are the theoretical fits to the experimental data points (circles). The vertical scales are again different for different curves, and the zeros have been shifted by different amounts.

Each data point in Fig. 11 represents approximately ten minutes of integration time. It must be pointed out that owing to small intensity of the fluorescence, great care had to be taken to reduce any direct leakage of radiation from the lamp to the photomultiplier tube. This is especially important since some of the lower resonance lines from the lamp are many orders of magnitude more intense than the higher resonance lines. The contribution of the lower resonance lines to fluorescence which might lie within the passband of the infrared filter was checked by introducing additional filters in front of the uv filter and was found to be negligible. A small direct leakage of the light was measured with an empty cell of identical dimensions and was corrected for. The observed magnitude of the polarization of the fluorescent radiation from the third excited S states ranged from about 5.5% at low magnetic fields to about 12.5% at high fields for both rubidium (6071 Å) and cesium (6355 Å) as shown in Table III. The quarter-wave plate for the visible wavelengths had a retardation value of (1400

± 200) Å. The uv quarter-wave plate had a retardation value of 900 Å for all eight states that have been investigated.

We have found the intensity of our lamp to be very stable. The effect of any small fluctuations or drifts in the intensity of the lamp are minimized by recording both the lock-in amplifier signal and the total fluorescent intensity simultaneously. The lock-in signal is then normalized.

The results of the hfs measurements are listed in Table IV. We are able to get consistent results to better than the quoted errors. However, we have quoted somewhat larger errors to account for any small systematic deviation between theory and experiment. Such systematic errors could be caused, for example, by depolarizing collisions in the excited states. The effect of nuclear spin will then be different at different magnetic fields, as the nuclear spin will tend to regenerate the electronic polarization at low magnetic fields. We have made every effort to operate below temperatures at which noticeable depolarization sets in. Systematic errors could also be caused by the magnetic scanning of the absorption lines at high external magnetic fields. In the case of Rb⁸⁷ and Cs¹³³ we do not have enough magnetic field to decouple *I* and *J* in the second excited states, as is evident from Fig. 10. At higher magnetic fields, the magnetic scanning of the absorption lines becomes particularly troublesome. We are therefore not sure that our results are not biased because of the limited field range. We have therefore quoted larger error bars on the results

TABLE IV. A list of the experimental and theoretical values of the hfs intervals. Column 3 shows the experimental values, while columns 4–6 show the values calculated from Fermi-Segré formula (Ref. 19), semiempirical formula (Ref. 18), and those calculated from relativistic Hartree-Fock theory (Ref. 20), respectively. The experimental ground-state hfs intervals were taken from Kopfermann (Ref. 18).

Element	State	$\Delta\nu_{(\text{exp})}$ (MHz)	$\Delta\nu_{\text{FS}}$ (MHz)	$\Delta\nu_{\text{se}}$ (MHz)	$\Delta\nu_{\text{RHF}}$ (MHz)
K ³⁹	4 ² S _{1/2}	461.7	482.4	496.8	368.98
	6 ² S _{1/2}	46 ± 2 ^a	45.33	46.69	
K ⁴¹	4 ² S _{1/2}	254.0	264.1	272.0	
	6 ² S _{1/2}	26 ± 2 ^a	25.22	25.97	
Rb ⁸⁵	5 ² S _{1/2}	3035.7	2809.4	3259.0	2380.62
	7 ² S _{1/2}	270 ± 10 ^a	268.8	311.8	
		278 ± 5 ^b			
Rb ⁸⁷	8 ² S _{1/2}	135 ± 15 ^a	133.5	154.9	
	5 ² S _{1/2}	6834.7	6349.6	7365.2	
		7 ² S _{1/2}	565 ± 60 ^a	606.1	703.2
Cs ¹³³	8 ² S _{1/2}	623 ± 7 ^b			
		290 ± 20 ^a	301.6	349.8	
	6 ² S _{1/2}	9192.6	6944.4	9374.9	6733.80
	9 ² S _{1/2}	680 ± 120 ^a	683.1	922.2	
	405 ± 30 ^a	343.2	463.2		

^aResults of the decoupling measurements.

^bResults of the rf spectroscopic measurements.

for these states. We have made no measurements on the first excited S states of these elements, because the transitions from these states to the lower P states lie well in the infrared region of the spectrum and cannot be detected by conventional photo-multiplier tubes.

Column 4 in Table IV shows the values of the hyperfine structure calculated from the Fermi-Segré formula. The Fermi-Segré formula may be written as¹⁹

$$\Delta\nu = \frac{8}{3} \frac{cR_\infty \alpha^2 Z g_I (I + \frac{1}{2})}{n_0^3 (M/m)} \left(1 - \frac{d\sigma}{dn} \right) \quad (35)$$

for the $S_{1/2}$ state of a neutral alkalilike atom. Here $\Delta\nu$ is the hyperfine-structure interval, n_0 is the effective quantum number of the state, and g_I and I are the nuclear g factor and the nuclear spin, respectively; σ is the Rydberg correction term. All the other quantities have their usual meaning. The term value T of a state with principal quantum number n is given by the Rydberg-Ritz formula (for neutral atoms)

$$T = R_\infty / n_0^2 = R_\infty / (n - \sigma)^2. \quad (36)$$

Both n_0 and $(d\sigma/dn)$ are determined from the known spectroscopic term values. Certain approximations have been made in the derivation of Eq. (35). A modified expression for $\Delta\nu$ can be written as¹⁸

$$\Delta\nu = \frac{8}{3} \frac{cR_\infty \alpha^2 Z g_I (I + \frac{1}{2})}{n_0^3 (M/m)} \left(1 - \frac{d\sigma}{dn} \right) \times F_r(j, Z)(1 - \delta)(1 - \epsilon), \quad (37)$$

which we shall refer to as the semiempirical formula. In the derivation of expression (35) only the

“large” part of the Dirac eigenfunction is used, which is equivalent to neglecting terms of order $\alpha^2 Z^2$. These terms become increasingly important for heavier elements, therefore all four components of the Dirac eigenfunctions must be taken into account for these elements. The term $F_r(j, Z)$ represents this correction. Moreover, in the derivation of Eq. (35), it has been assumed that the nucleus is both a point charge and a point magnet. Actually, the distribution of nuclear charge and that of magnetic moment within the finite nuclear volume must be considered. The terms $(1 - \delta)$ and $(1 - \epsilon)$ represent the corrections due to the finite extent of the nuclear charge and that of the nuclear magnetic moment, respectively. These correction factors have been calculated by various authors and have been listed by Kopfermann.¹⁸ Column 5 in Table IV shows values of the hyperfine-structure interval $\Delta\nu$ calculated from the semiempirical formula. It will be noticed that the experimental values of the hyperfine-structure intervals in the ground states of alkali atoms agree quite well with the semiempirical formula. However, for excited S states the experimental values seem to lie much closer to the (unmodified) Fermi-Segré formula. The values of the hyperfine-structure intervals have been calculated for the ground states of alkali atoms using relativistic Hartree-Fock theory²⁰ and are listed in Column 6 of Table IV.

We have recently completed radio-frequency spectroscopy experiments on the $7^2S_{1/2}$ states of Rb⁸⁵ and Rb⁸⁷. The preliminary results of these measurements are shown in the third column of Table IV and are seen to be in good agreement with the decoupling results.

†Work supported by the Joint Services Electronics Program (U. S. Army, U. S. Navy, and U. S. Air Force) under Contract No. DAAB07-69-C-0383, and in part by the U. S. Air Force Office of Scientific Research under Contract No. AFOSR-68-1454B.

¹S. Chang, R. Gupta, and W. Happer, Phys. Rev. Letters **27**, 1036 (1971).

²G. Zu Putlitz, Ergeb. Exakt. Naturw. **37**, 105 (1965).

³R. W. Schmieder, A. Lurio, and W. Happer, Phys. Rev. A **2**, 1216 (1970).

⁴Y. Archambault, J. P. Descoubes, M. Priou, A. Omont, and J. C. Pebay-Peyroula, J. Phys. Radium **21**, 677 (1960).

⁵R. Gupta, S. Chang, and W. Happer, Bull. Am. Phys. Soc. **15**, 1508 (1970).

⁶M. Pavlovic and F. Laloč, J. Phys. (Paris) **31**, 173 (1970).

⁷B. P. Kibble and S. Pancharatnam, Proc. Phys. Soc. (London) **86**, 1351 (1965).

⁸R. L. Smith and T. G. Eck, Phys. Rev. A **2**, 2179 (1970).

⁹W. Hanle, Z. Physik **30**, 93 (1924).

¹⁰A. Ellet and N. P. Heydenburg, Phys. Rev. **46**, 583

(1934); N. P. Heydenburg, *ibid.* **46**, 802 (1934).

¹¹R. Prepost, V. W. Hughes, and K. Ziock, Phys. Rev. Letters **6**, 19 (1961).

¹²P. A. Franken, Phys. Rev. **121**, 508 (1961).

¹³T. G. Eck (private communication); T. G. Eck, L. L. Foldy, and H. Wieder, Phys. Rev. Letters **10**, 239 (1963).

¹⁴R. Gupta, S. Chang, and W. Happer, Bull. Am. Phys. Soc. **17**, 476 (1972).

¹⁵W. Happer and B. S. Mathur, Phys. Rev. **163**, 12 (1967).

¹⁶S. Chang, thesis (Columbia University, 1972) (unpublished).

¹⁷G. S. Kwater and T. G. Meister, Vestn. Leningr. Univ. **9**, 137 (1952); B. Warner, Monthly Notices Roy. Astron. Soc. **139**, 115 (1968); P. M. Stone, Phys. Rev. **127**, 1151 (1962).

¹⁸H. Kopfermann, *Nuclear Moments* (Academic, New York, 1968).

¹⁹E. Fermi and E. Segré, Z. Physik **82**, 729 (1933).

²⁰L. Tterlikkis, S. D. Mahanti, and T. P. Das, Phys. Rev. **176**, 10 (1968); T. Lee, N. C. Dutta, and T. P. Das, Phys. Rev. A **1**, 995 (1970).